How to cite: *Angew. Chem. Int. Ed.* **2024**, *63*, e202314638
doi.org/10.1002/anie.202314638

Membranes | Very Important Paper

Shearing Liquid-Crystalline MXene into Lamellar Membranes with Super-Aligned Nanochannels for Ion Sieving

Lingzhi Huang[+], *Haoyu Wu*[+], *Li Ding*,* *Jürgen Caro*, *and Haihui Wang**

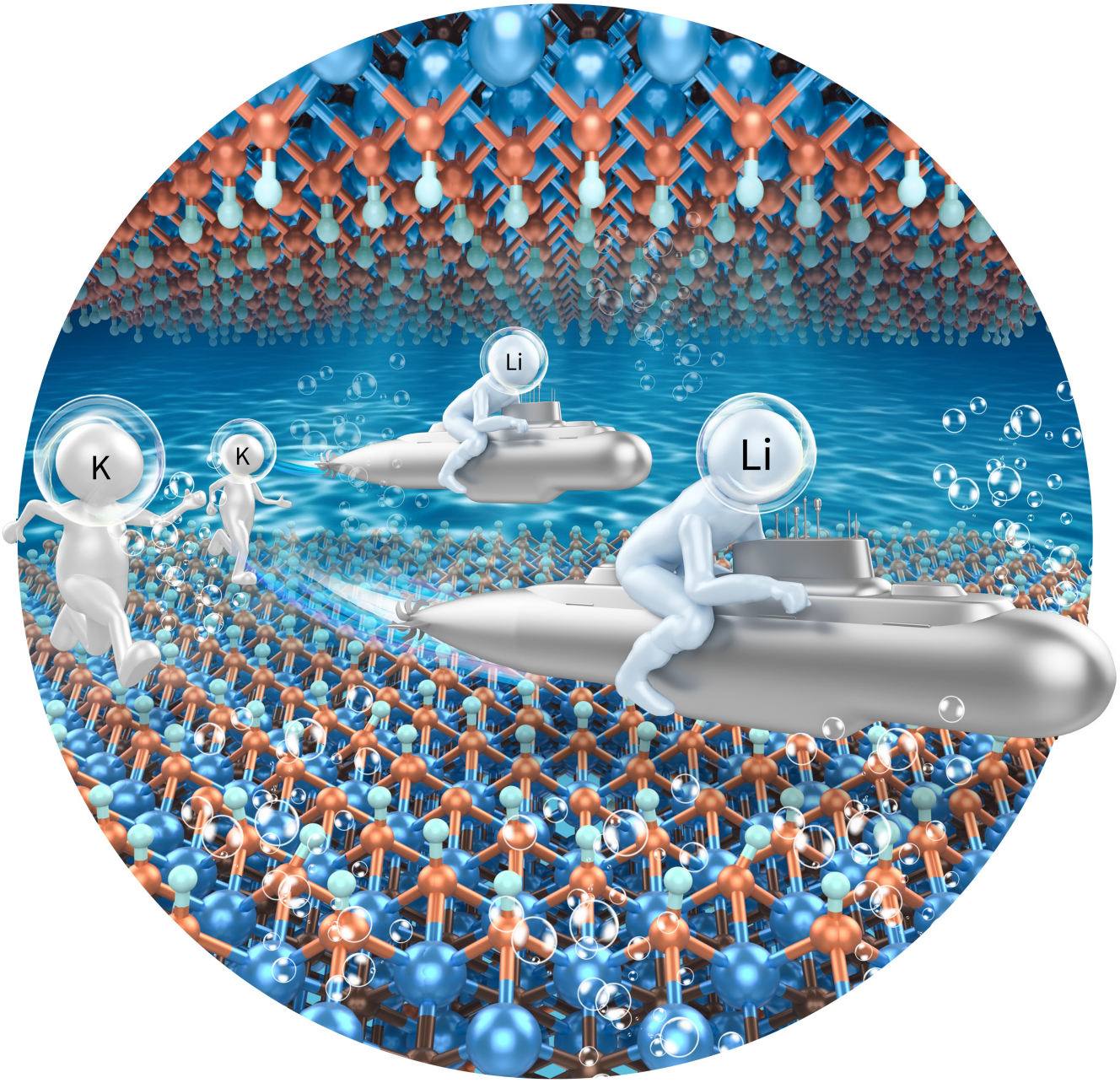

Abstract: Ion-selective membranes are crucial in various chemical and physiological processes. Numerous studies have demonstrated progress in separating monovalent/multivalent ions, but efficient monovalent/monovalent ion sieving remains a great challenge due to their same valence and similar radii. Here, this work reports a two-dimensional (2D) MXene membrane with super-aligned slit-shaped nanochannels with ultrahigh monovalent ion selectivity. The MXene membrane is prepared by applying shear forces to a liquid-crystalline (LC) MXene dispersion, which is conducive to the highly-ordered stacking of the MXene nanosheets. The obtained LC MXene membrane (LCMM) exhibits ultrahigh selectivities toward Li^+/Na^+, Li^+/K^+, and Li^+/Rb^+ separation (≈ 45, ≈ 49, and ≈ 59), combined with a fast Li^+ transport with a permeation rate of $\approx 0.35\ mol\,m^{-2}\,h^{-1}$, outperforming the state-of-the-art membranes. Theoretical calculations indicate that in MXene nanochannels, the hydrated Li^+ with a tetrahedral shape has the smallest diameter among the monovalent ions, contributing to the highest mobility. Besides, the weakest interaction is found between hydrated Li^+ and MXene channels which also contributes to the ultrafast permeation of Li^+ through the super-aligned MXene channels. This work demonstrates the capability of MXene membranes in monovalent ion separation, which also provides a facile and general strategy to fabricate lamellar membranes in a large scale.

Introduction

Lithium, is one of the most prominent elements in organic synthesis, nuclear industry, and energy storage.[1] With increasing industrialization and the soaring trend of global electrification in the past decades, the consumption of lithium resources increased dramatically. More than 60 % of the world's lithium resources are stored in salt lakes.[2] Efficient separation and purification techniques are needed for lithium extraction.[3] Among the various extraction methods, membrane technology features the merits of high efficiency and low carbon emission,[4] showing great promise in high-performance and sustainable lithium extraction. Typically, extracting lithium from salt lakes mainly involves monovalent/divalent ions separation (such as Li^+ and Mg^{2+}) and monovalent/monovalent ion separation (such as Li^+/Na^+).[5] Due to the distinct differences in size and charge between Li^+/Mg^{2+}, many kinds of membranes[6] have realized efficient Li^+/Mg^{2+} separation. For example, a modified polyamide (PA) membrane exhibits a Li^+/Mg^{2+} separation factor of 60.1 when increasing the surface charge density.[6d] Furthermore, a covalent organic frameworks (COF) membrane with abundant hydroxyl sites shows an ultrahigh Li^+/Mg^{2+} selectivity of ≈ 217.[6a] Despite the efficient separation of Li^+/Mg^{2+}, these membranes failed to separate monovalent ions due to the same valence and similar diameters of Li^+ (7.64 Å), Na^+ (7.16 Å), K^+ (6.62 Å), and Rb^+ (6.58 Å) in the hydrated states.[7] Recently, researchers provided a new perspective in achieving high-performance monovalent ion separation showing that in constraint geometries such as nanopores, the alkali ions become partially dehydrated.[8] Interestingly, the partially dehydrated Li^+ ions have a higher mobility than the other partially dehydrated alkali ions.[8–9] For example, a metal–organic frameworks (MOF) membrane[9b] with a window size of 3.4 Å could selectively sieve Li^+ with a Li^+/K^+ selectivity of 2.2. The hydrated Li^+ tends to dehydrate when passing through the MOF window, and the partially dehydrated Li^+ has the smallest diameter, contributing to the faster permselective transport over Na^+, K^+, and Rb^+. Moreover, the same phenomenon was also observed in charged two-dimensional (2D) vermiculite nanochannels (4.3 Å),[9a] in which the partially dehydrated Li^+ diffuses faster than Na^+ and K^+ resulting in Li^+/Na^+ and Li^+/K^+ selectivities of 1.26 and 1.59. However, the monovalent ion sieving performances of these membranes are still unsatisfying with Li^+/M^+ selectivities < 5 (M represents Na, K, and Rb). Therefore, developing an advanced membrane material for high-performance monovalent ion sieving is still challenging.

MXenes, an emerging family of 2D nanomaterials and a rising star for the fabrication of lamellar membranes, are derived from layered MAX-phase (e.g. Ti_3AlC_2) materials.[10] MXenes have the general formula $M_{n+1}X_nT_x$, where M represents an early transition metal,[10a] X denotes carbon and/or nitrogen, T refers to the terminating surface functional groups (−OH,=O, and –F), and *n* varies from 1 to 4. MXenes combine the advantages of good flexibility, diversity, tunable functionalities, and hydrophilicity.[11] Over the last decade, MXenes have been widely processed into lamellar membranes which have been successfully evaluated in gas separation,[12] desalination,[13] and nanofluidic devices.[14] In fact, the interlayer channel, i.e., the empty space between the MXene nanosheets of the wet MXene membranes is around 6 Å.[6b,13] This size signifies that hydrated Li^+ needs partial dehydration to enter the MXene channels, while the dehydrated Li^+ has a smaller diameter than the other dehydrated alkali metal ions, revealing great prom-

[*] L. Huang,[+] H. Wu,[+] L. Ding, H. Wang
Beijing Key Laboratory for Membrane Materials and Engineering, Department of Chemical Engineering, Tsinghua University
Beijing, 100084 (China)
E-mail: celiding@tsinghua.edu.cn
cehhwang@tsinghua.edu.cn

J. Caro
Institute of Physical Chemistry and Electrochemistry, Leibniz University Hannover
Callinstrasse 3 A, 30167 Hannover (Deutschland)

[+] These authors contributed equally to this work.

ise for highly-efficient Li^+/M^+ sieving.[9] However, to the best of our knowledge, only a few studies report high-performance monovalent ion separation using MXene membranes. These observations are based on the presence of defects or disordered stackings in those MXene membranes, which obscured their intrinsic properties.[15]

Herein, we report defect-free MXene membranes with super-aligned nanochannels by applying shear forces to a liquid-crystalline (LC) MXene nanosheet dispersion (Figure 1a and Figure S1). The LC MXene nanosheet dispersion shows the fluidity of liquids and the long-range order of crystals. The prepared supported membrane layer shows excellent in-plane stacking order and precise interlayer spacing of ≈6 Å. The obtained LC MXene membrane (LCMM) exhibits ultrahigh selectivities toward Li^+/Na^+, Li^+/K^+, and Li^+/Rb^+ (≈45, ≈49, and ≈59, respectively) and a high permeation rate of Li^+ (≈0.35 mol $m^{-2} h^{-1}$), outperforming the state-of-the-art membranes. Molecular dynamics (MD) simulations and density functional theory (DFT) results confirm the high mobility of Li^+ ions. This work demonstrates the importance of constructing uniform nanochannels of MXene membranes and provides insights into the design of high-performance ion sieving membranes.

Results and Discussion

According to the Onsager theory, 2D nanosheet dispersion can form liquid crystals at sufficiently large sizes of the nanosheets and sufficiently high concentrations.[16] To prepare large-size MXene nanosheets, a preselecting

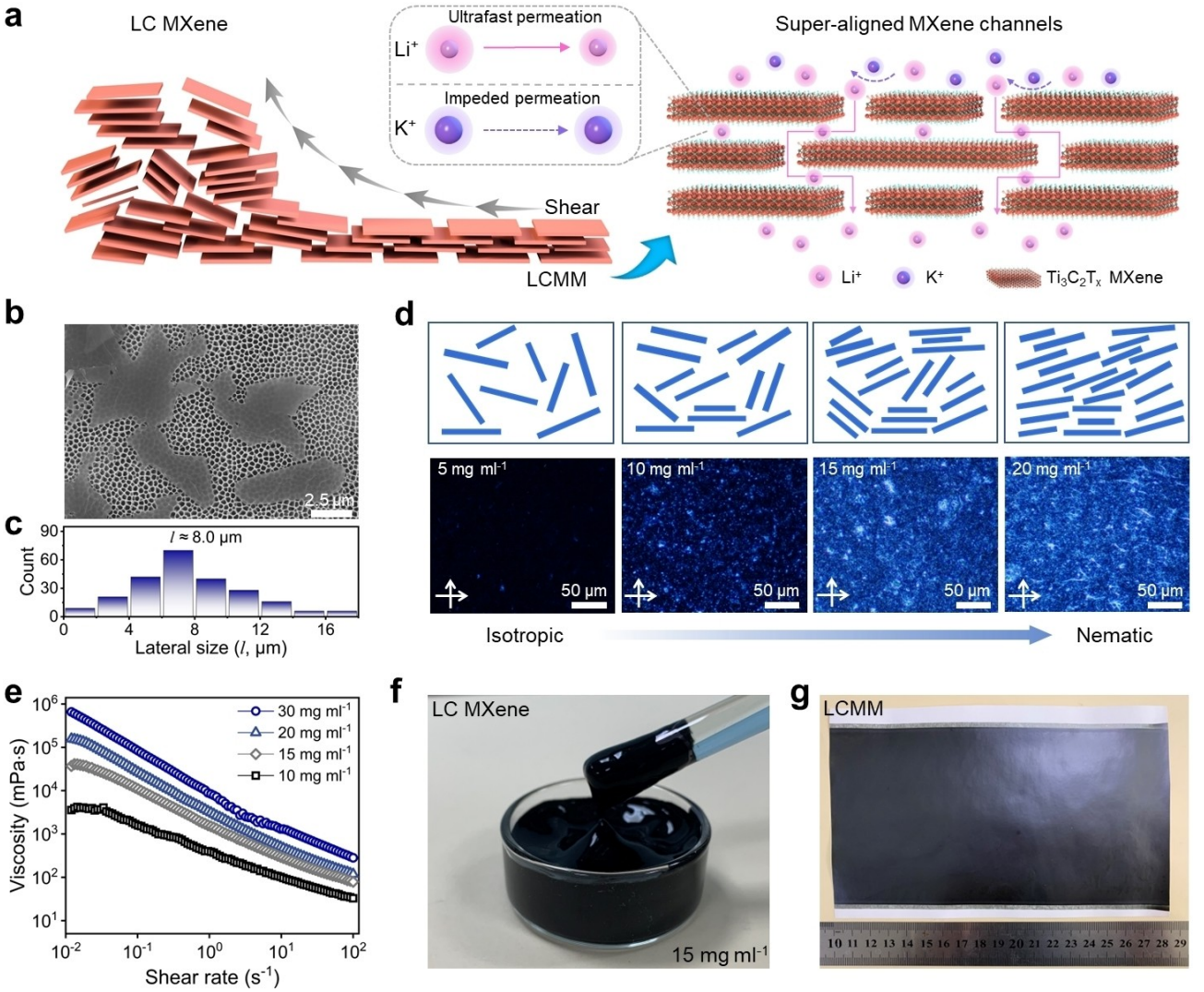

Figure 1. Preparation of the LCMM. (a) Schematic illustration of the fabrication of LCMM by shearing LC MXene nanosheets and the corresponding separation process. (b) Scanning electron microscopy (SEM) images of MXene nanosheets and (c) size distribution based on 200 nanosheets. (d) Polarized optical microscopy (POM) images of MXene dispersions for the concentrations of 5, 10, 15, and 20 mg ml^{-1} with the illustrations of MXene nanosheets changing from isotropic to nematic state. (e) Viscosity versus shear rate for MXene nanosheet dispersions at different concentrations. Digital photos for (f) the viscous LC MXene dispersions at 15 mg ml^{-1} and (g) the as-prepared LCMM.

method[17] was used (Supporting Information and Figure S2). Briefly, the small-sized MAX (Ti_3AlC_2) powder particles stay in solution while the large-sized ones form a sediment. After three cycles, the remaining large-sized MAX particles were used in the etching process. The $Ti_3C_2T_x$ MXene nanosheets (Figure S3–S7) with a large aspect ratio could be obtained by a modified etching method.[18] As shown in Figure 1b–c, the MXene nanosheets have an average lateral size of 8 μm, with an aspect ratio (*l/d)* over 10^3, which is also proved by the dynamic light scattering (DLS) (Figure S8). The typical Tyndall effect and the Zeta potential analysis (Figure S9–S10) demonstrate the excellent dispersity and stability of the MXene nanosheet dispersions. Figure 1d presents the corresponding polarized optical microscopy (POM) images of MXene nanosheet dispersions at different concentrations. When the concentration was 5 mg ml^{-1}, the MXene dispersion formed as an isotropic phase. A clear change in birefringence occurs at a concentration of 10 mg ml^{-1}, indicating the formation of a nematic phase dispersion. As depicted in Figure 1d, the MXene dispersion thoroughly transformed from an isotropic state to a nematic state when the concentration is over 15 mg ml^{-1}, behaving as an LC dispersion. Furthermore, the rheological properties[19] of MXene dispersions were also investigated. The viscosity of the MXene dispersion increases drastically with rising concentrations and decreases with increasing the shear rate (Figure 1e and Figure S11–S12), which is consistent with previous reports.[20] The prepared LC MXene dispersion (15 mg ml^{-1}) is highly viscous and shiny (Figure 1f). By using a blade-coating method applying shear force to the LC MXene dispersion, a defect-free shiny metallic MXene membrane could be obtained on the porous Nylon support (Figure 1g).

The shear thinning behavior allows us to apply shear stress to align the MXene nanosheets in-plane and fabricate lamellar membranes with a superior arrangement of the nanosheets. A series of MXene membranes were prepared from MXene nanosheet dispersion of different concentrations, see Figure S13–S16. For comparison, we also prepared MXene membranes from the non-liquid-crystal MXene dispersion with a lower MXene concentration of 10 μg mL^{-1} (called NLCMM). The 3D atomic force microscope (AFM) images in Figure 2a–b intuitively present the topography difference between the LCMM and NLCMM. The roughness of the LCMM is as low as ≈60 nm over a large scale of 50 μm, much lower than that of the NLCMM with ≈600 nm surface roughness. The scanning electron microscopy (SEM) images also show that the LCMM possesses a much smoother surface without noticeable wrinkles compared to NLCMM (Figure 2c–d). The cross-sectional SEM images demonstrate the superior alignment of MXene nanosheets of LCMM, while the twisted wrinkles indicate the disordered stacking in NLCMM (Figure 2e–f), both membranes with a thickness of ≈1 μm. In addition, X-ray diffraction (XRD) was carried out to assess the crystalline order of the LCMM and NLCMM (Figure S17). As expected, the LCMM exhibits a much narrower and stronger (002) peak and a more pronounced (004) peak compared to the NLCMM. Besides, we studied the interlayer spacing of wet and dry states of the membranes, as shown in Figure 2g. The normalized XRD patterns indicate that the interlayer spacing increased from ≈3 Å (dry state) to ≈6 Å (wet state) due to the intercalation of water molecules.[13] To further study the difference between the LCMM and NLCMM, we carried out a series of characterizations and found that they are almost identical in their physicochemical properties (Figure S18–S21) except for the nanosheet stacking order.

We have used two experimental methods to characterize the stacking order of nanosheets in the membranes using (i) a polarization camera and (ii) 2D wide-angle X-ray diffraction (WAXD). Polarized light imaging can be used to study the local orientation by imaging the slow axis of alignment of the MXene nanosheets in the plane of the membrane. Equipped with the LPS Abrio imaging system, the polarization camera can provide falsely colored polarized light images, where different hues of color represent the azimuth more visibly, which has been widely used to investigate the order parameter characterizations for liquids and films.[21] As displayed in Figure 2h–i, the LCMM shows a uniform hue over hundreds of micrometers, while the colorful polarized image of the NLCMM demonstrates a distributed hue. Since the color legend is a guide relating hue to azimuth, we displayed the polar histograms of the azimuth angles of the LCMM (Figure 2j) and NLCMM (Figure 2k). The bottom of the images shows the vector overlay of the azimuth at regular grid points. Apparently, the LCMM demonstrates a better orientation. A scalar parameter, S (for calculation details, see the Supporting Information), representing the distribution of the azimuthal angles in the x-y plane, was adopted to describe the in-plane nanosheet alignment of the MXene membranes. The LCMM exhibits an S value of ≈0.99 (calculation based on 1000 pixels), indicating the perfect in-plane stacking behavior. However, the NLCMM exhibits an S value of ≈0.31, implying a poor nanosheet alignment.

We also used 2D-WAXD measurements to elucidate the different stacking of the nanosheets in LCMM and NLCMM. Accordingly, a more concentrated and intensive scattering for the (002) plane of the LCMM is observed in the WAXD images (Figure 2l and Figure S22), demonstrating a higher in-plane uniformity in LCMM. The WAXD data of the (002) plane was converted into 1D azimuthal plots (Figure 2l) to quantitatively compare the MXene nanosheet alignment in LCMM and NLCMM. The distribution of the azimuthal angle of the LCMM is narrower and more concentrated, as LCMM has a smaller full width at half maximum (FWHM). Moreover, we calculated the distribution of the inclination angle of the nanosheets deviated from the (002) plane based on the azimuthal data, which intuitively verifies the super-aligned structure of LCMM (Figure S23). Notably, these results strongly confirm that using LC MXene nanosheet dispersion and applying shear stress is advantageous to prepare membranes with ultrahigh alignment.

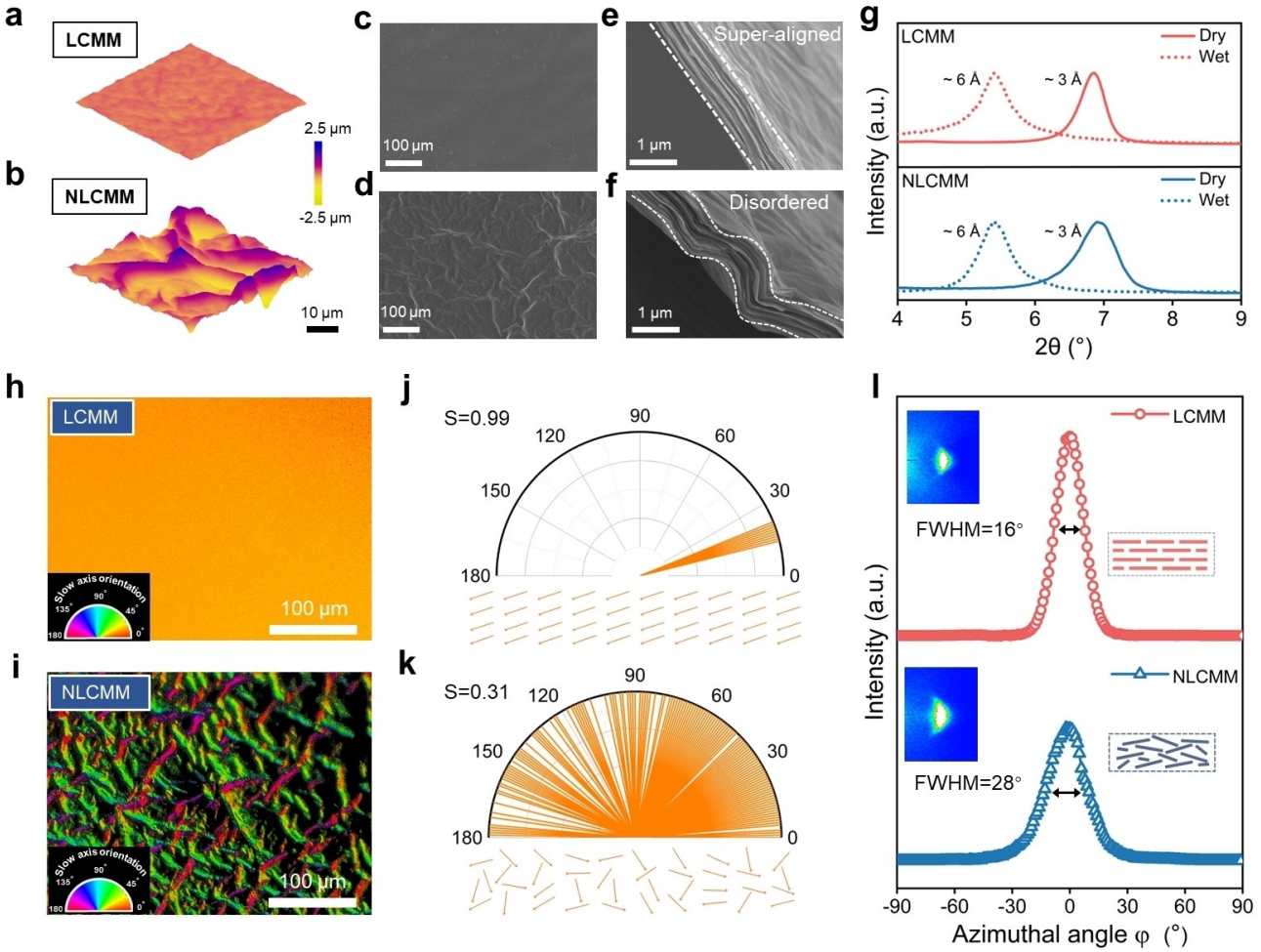

Figure 2. Characterizations. 3D AFM images of (a) LCMM and (b) NLCMM. Surface SEM images of (c) LCMM and (d) NLCMM. Cross-sectional SEM images of (e) LCMM and (f) NLCMM. (g) XRD patterns of LCMM and NLCMM in dry and wet states. Polarized light images of (h) LCMM and (i) NLCMM. The color legend is a guide relating hue to azimuth (expressed around the circumference of the semicircle) and brightness to apparent retardance (expressed radially in nm). Polar histograms of the azimuth angles and the in-plane order parameter for (j) LCMM and (k) NLCMM. The bottom of the images shows the vector overlay of the azimuth at regular grid points. (l) Azimuthal angle plot of the membranes. Insets are the 2D WAXD patterns (left) of the LCMM and NLCMM and the corresponding schematic illustration of MXene nanosheets in the membrane (right).

We investigated permeation rates of the monovalent ions (Li^+, Na^+, K^+, and Rb^+) through LCMM and NLCMM by using a homemade U-shaped device (Figure S24) with 0.2 M salt solution as feed. At first, we evaluated the LCMM and found that the number of permeated ions increases linearly with time by recording the conductivity on the permeation side (Figure 3a). Accordingly, the permeation rate of Li^+ is as high as $\approx 0.35\ mol\,m^{-2}h^{-1}$, while for Na^+, K^+, and Rb^+, the values are much lower and amount ≈ 0.0079, 0.0070, and $0.0057\ mol\,m^{-2}h^{-1}$, respectively. However, for the NLCMM, the permeation rate of Li^+ is as low as $\approx 0.025\ mol\,m^{-2}h^{-1}$ (Figure 3b). This interesting phenomenon is probably associated with the MXene nanosheet stacking order of the membranes. The super-aligned structure endows the LCMM with a precise channel size of ≈ 6 Å, while disordered nanosheet stacking might lead to a wider distribution of channel sizes for NLCMM (Figure S25–S26 also provide the free-spacing changes of LCMM and NLCMM in different solutions). The uniform MXene channels of LCMM build up a fast and straightforward pathway for Li^+, while the randomly distributed channels of NLCMM provide a slow and tortuous pathway. This brings an enormous difference in the ideal selectivity of Li^+/M^+ between LCMM and NLCMM. As displayed in Figure 3c, for the LCMM, the ideal selectivity of Li^+/Na^+, Li^+/K^+, and Li^+/Rb^+ are ≈ 45, ≈ 49, and ≈ 59, respectively. But for the NLCMM, the selectivities of Li^+/Na^+, Li^+/K^+, and Li^+/Rb^+ are as poor as ≈ 2.9, ≈ 3.9, and ≈ 4.1, respectively. Certainly, the porous Nylon substrate does not contribute to any selectivity (Figure S27). We also used the binary system with the molar ratio of $Li^+/M^+ = 1$ as feed to further explore the separation performance of the LCMM and NLCMM. The permeation rates of binary ions were calculated from concentration analysis by inductively coupled plasma mass spectrometry (ICP-

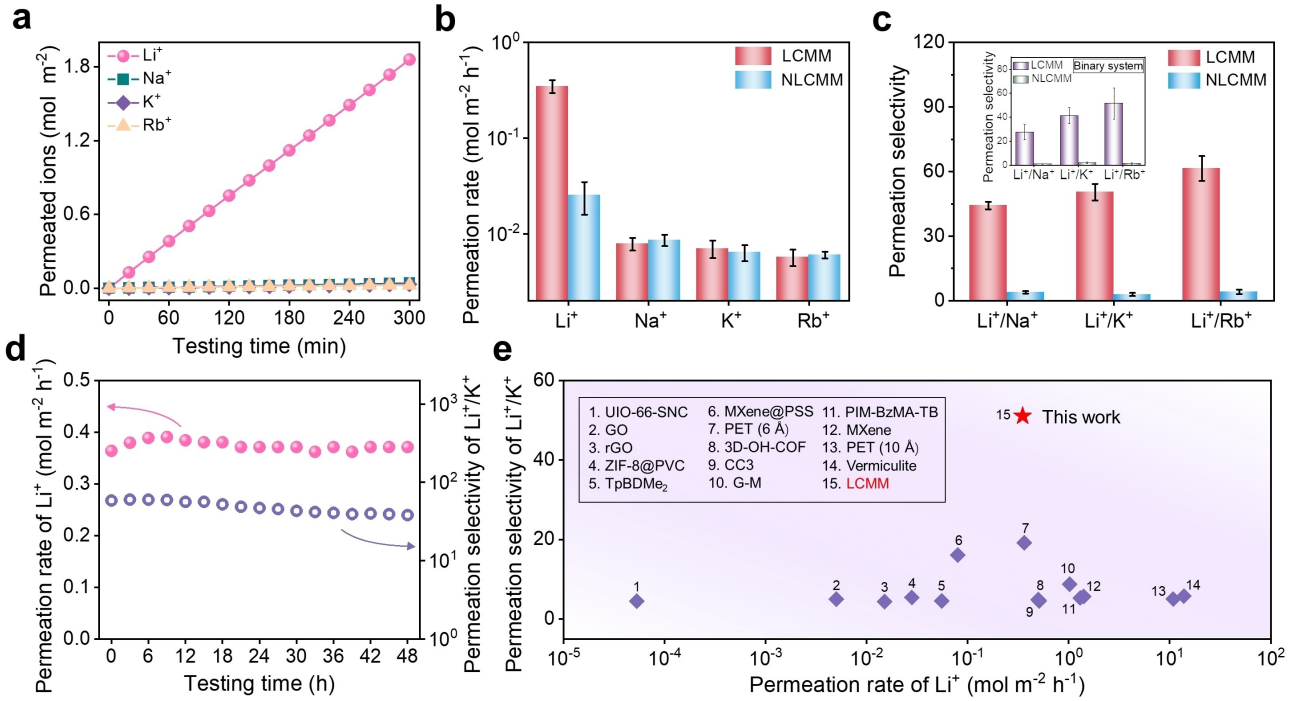

Figure 3. Ion separation performance. (a) Permeated ions (Li^+, Na^+,/K^+, and Rb^+) through the LCMM as a function of testing time. (b) Comparisons of the permeation rates through LCMM and NLCMM. (c) Permeation selectivity of Li^+/Na^+, Li^+/K^+, and Li^+/Rb^+ through LCMM and NLCMM. Inset is the binary ion selectivity of LCMM and NLCMM. (d) Long-term stability of the LCMM. (e) Comparisons of Li^+/K^+ selectivity of various membranes.[6b,e,7b,c,d,8,23–24]

MS) (Table S1). The selectivity of Li^+/Na^+, Li^+/K^+, and Li^+/Rb^+ is ≈27, ≈41, and ≈52. A slight decrement in selectivity is observed in comparison with the ideal selectivities due to the competitive effect of cations,[22] as displayed in Figure 3c (inset). Further, the permeation rate of Mg^{2+} and the selectivity of Li^+/Mg^{2+} are also given in Figure S28. LCMM and NLCMM exhibit higher selectivity for Li^+/Mg^{2+} compared with other monovalent Li^+/M^+ pairs. Interestingly, despite the huge difference in the permeation rate, both LCMM and NLCMM demonstrate a preferential transport of Li^+, which agrees with previous reports.[6b,23] These results demonstrate that MXene membranes favor the permeation of Li^+ over other monovalent cations, which might be due to the weak interaction between Li^+ and MXene surface, while other ions with larger diameters tend to become adsorbed on MXenes and thus hindering their transport.

Moreover, a long-term test was carried out to examine the stability of LCMM. As shown in Figure 3d, no apparent decline is observed in the permeation rate of Li^+ and the permeation selectivity of Li^+/K^+ in the 48-hour test. This experiment not only suggests that LCMM provides ultrafast and selective nanochannels for Li^+ but also implies the superior stability of LCMM. As a step further, to assess the uniformity of the prepared LCMM, we chose a large-area LCMM and selected different areas for the ion permeation test. As displayed in Table S2, the results demonstrate a remarkable uniformity of a large-area LCMM, further proving that the shear-aligned method can be scaled up to fabricate lamellar membranes without sacrificing separation performance.

Due to their same valence and similar ionic radii (Table S3), the effective separation of monovalent ions is very challenging. Various materials have been processed recently into membranes aiming at high-performance monovalent cation separation. However, only a few membranes achieved a satisfying selectivity,[6b,8] mostly lower than 5, as shown in Figure 3e. For example, the selectivity of Li^+/K^+ of the nacre-like GO-MXene composite membrane is 4.8. Obviously, our LCMM outperforms the state-of-art membranes in the Li^+/K^+ selectivity. The detailed comparisons are provided in Table S4.

To elucidate the ion sieving mechanism, we performed density functional theory (DFT) and classical molecular dynamics (MD) simulations of the ion hydration states and ion transport through simulated LCMM and NLCMM channels (detailed calculations are provided in Supporting Information). First, the equilibrium states of hydrated Li^+, Na^+, K^+, and Rb^+ in the MXene channels of 6 Å width are presented in Figure 4a. These alkali ions show different hydration states in the 2D confined channels, which are related to their bare ionic diameter and interaction with the MXene surface. For example, the smallest Li^+ ion is hydrated with 4 water molecules in the shape of a tetrahedron, while the larger K^+ is hydrated with 6 water molecules in the shape of an octahedron. Notably, the ions' hydration states are closely associated with their mobility in the slit channels. Therefore, to comprehensively analyze the hydration states of ions in

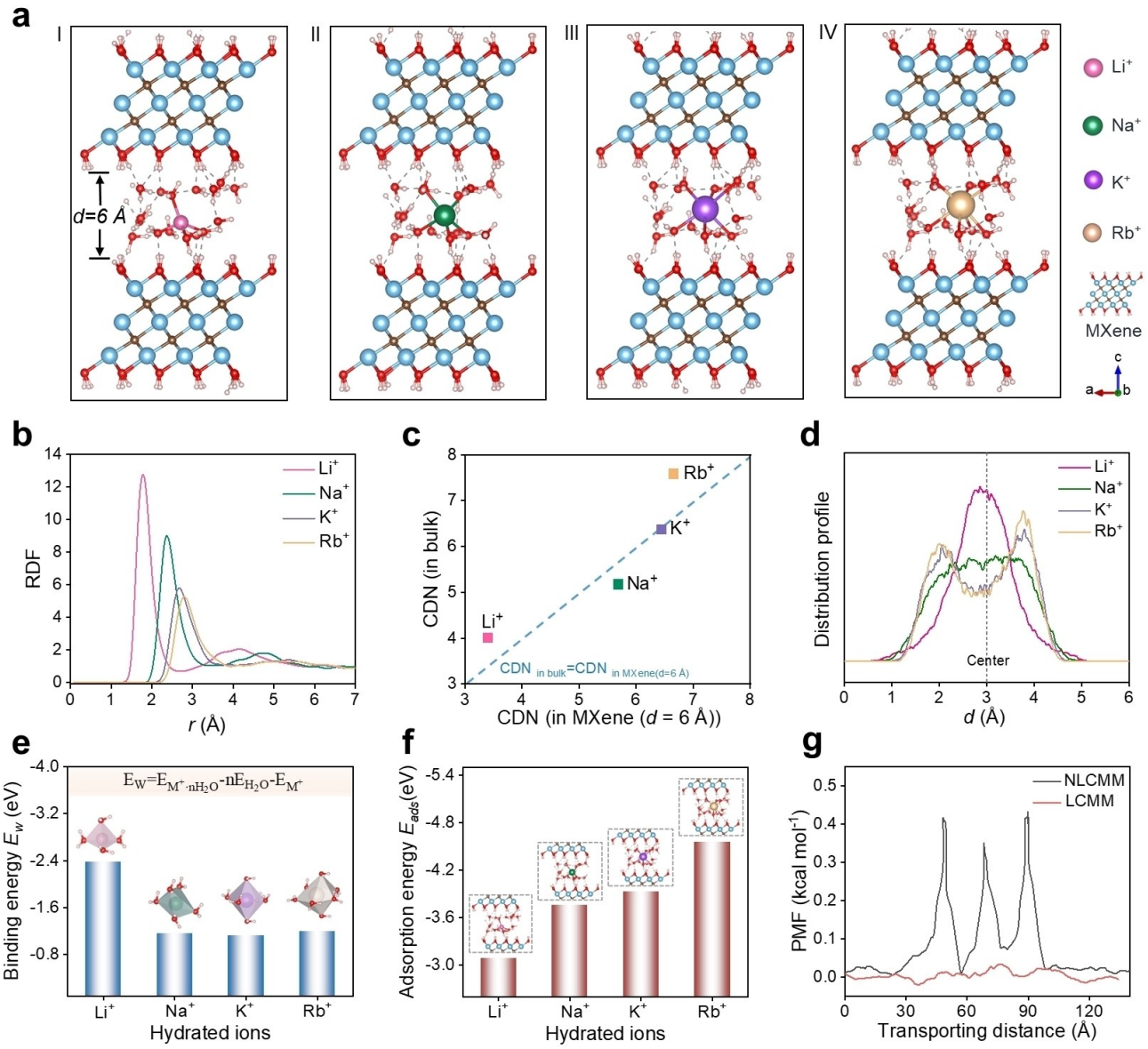

Figure 4. Theoretical calculations. (a) Equilibrium states of Li^+, Na^+, K^+, and Rb^+ in MXene 2D channels at a width of 6 Å. (b) Radius distribution function (RDF) of water molecules around Li^+, Na^+, K^+, and Rb^+ ions in MXene 2D channels at a width of 6 Å. (c) Comparison of coordination number (CDN) of ions in bulk solution and in MXene channels (d = 6 Å). (d) Distribution profile of Li^+, Na^+, K^+, and Rb^+ ions in MXene channels (d = 6 Å). (e) Binding energy of the hydrated ions in MXene channels, $Li^+{\cdot}4H_2O$, $Na^+{\cdot}5H_2O$, $K^+{\cdot}6H_2O$, $Rb^+{\cdot}7H_2O$, respectively. (f) Adsorption energy of the hydrated ions with MXene channels (d = 6 Å). (g) The calculated potential of the mean force (PMF) of $Li^+{\cdot}4H_2O$ through LCMM and NLCMM.

MXene channels, we performed the water's radial distribution functions (RDF) by quantifying the relative positions between the ions and the oxygen atom of water, as shown in Figure 4b. Apparently, the Li^+ ion exhibits the shortest cation-water distance and consequently the most compact structure. Compared with the bulk solutions, the first peaks in the RDF profile of hydrated ions inside the slit-shaped pores look identical describing the 1st hydration shell (Figure S29). However, the second peaks are much flatter, which means that the interaction of cations with water in the 2nd hydration shell is getting much weaker, especially for the Li^+ ion. Therefore, we can deduce that the hydrated Li^+ (7.64 Å) gets partially dehydrated to enter the MXene channels (d = 6 Å). To intuitively understand the dehydration process, the coordination number (CDN) of these ions in both bulk solutions and in MXene nanochannels are studied,[25] as presented in Figure 4c. As for the 1st hydration shell, the CDN of Li^+, Na^+, K^+, and Rb^+ change only a little. Accordingly, the CDN of Li^+ is ≈4, Na^+ is ≈5, K^+ is ≈6, and Rb^+ is ≈7 (Table S5). In the confined space of 2D channels, the formation of a 2nd hydration shell in the narrow pores is not possible for steric reasons. Surprisingly, the cation-water distance of the 1st shell increases

for all ions (Figure S30), and this might be attributed to the confined space in the MXene interlayer leading to a change in the geometry of the hydrated ions. Because of the narrow channels, the hydrated ions are deformed in the 2D direction. Converse to the situation in bulk solution, Li^+ ions exhibit the smallest diameter among these alkali ions in MXene channels of 6 Å distance. Furthermore, we track the ions moving in MXene channels and analyze their distribution profile (Figure 4d). Interestingly, different from other monovalent ions under study, Li^+ ions show a concentrated distribution at the center of the 6 Å MXene channel, while Na^+ shows a more even distribution and K^+, Rb^+ tends to reside close to the MXene surface. This suggests that $Li^+ \cdot 4H_2O$ with the smallest diameter is more likely to enter and then become transported through the 6 Å MXene channels compared with other monovalent ions such as K^+ or Na^+, which explains the high selectivity of LCMM.[26]

To figure out the difference in ions' mobility, we first computed the binding energy (Ew, $Ew=EM^+ \cdot nH_2O\text{-}nEH_2O\text{-}EM^+$, n represents the CDN of the hydrated M^+) of the hydrated ion cluster. We obtained the following ranking: Li^+ (−2.379 eV) > Na^+ (−1.507 eV) > K^+ (−1.118 eV) ≈ Rb^+ (−1.197 eV), as shown in Figure 4e and Figure S31. This finding indicates that the Li^+ hydrated with 4 water molecules exhibits the most stable structure with less possibility of exchange with surrounding water molecules, which favors the migration of Li^+ ion. Further, the adsorption energy (E_{ads}) between hydrated cations and MXene was calculated to demonstrate the capability of their diffusion in MXene channels. The E_{ads} values (Figure 4f) are ranked as below: Li^+ (−3.082 eV) > Na^+ (−3.756 eV) > K^+ (−3.932 eV) > Rb^+ (−4.550 eV), indicating that it is easiest for hydrated Li^+ to migrate through MXene channels due to the weakest interaction, which is also consistent with the fast permeation of Li^+ observed in experiments. However, the relatively stronger interaction of Na^+, K^+, and Rb^+ with the MXene channels might lead to strong adsorption at the MXene surface thus hindering their migration, which explains their slow transport. This finding is also consistent with their distribution profile in Figure 4d. It can be concluded that the interactions of alkali ions with the channel surface are quite different despite the same valence and similar radii, and this interaction dominates their transporting behavior in the confined nanochannels.

Further, we carried out a series of calculations to understand distinctly the different permeation rates of hydrated Li^+ ions in the LCMM and NLCMM. In contrast to the super-aligned channels in LCMM, the MXene channels were set with varying widths and angles to simulate the disordered MXene nanosheet stacking in NLCMM (as illustrated in Figure S32). The potential of the mean force (PMF) of hydrated Li^+ ions traveling through LCMM and NLCMM was computed, and the results are shown in Figure 4g. The PMF of hydrated Li^+ passing through the NLCMM shows a much higher energy barrier (0.40 kcal mol^{-1}) due to repeated ion dehydrations than through the LCMM (0.037 kcal mol^{-1}) with parallel MXene nanosheets, indicating the huge transport barrier in NLCMM channels. The narrow and random MXene channels build up an enormous steric barrier for ions to enter and become transported (detailed information is presented in Figure S33–S34), which might lead to the detour of hydrated ions from polyhedron (d = 6 Å) to planar (d = 3 Å) geometry and prolong the transport pathway. This model explains the experimentally observed low permeability of ions through NLCMM. Overall, our theoretical calculations reveal that the ultrahigh monovalent ion selectivity of the LCMM is attributed to two parts, one is the uniformly distributed size of the slit-shaped channels with d = 6 Å width in LCMM, and the other is the lowest adsorption energy of $Li^+ \cdot 4H_2O$ at MXene channels.

Conclusion

We have developed a lamellar MXene membrane with super-aligned nanochannels by applying shear stress on a LC MXene dispersion. The as-prepared LC MXene membranes show an ultrafast and selective transport of Li^+ over other monovalent ions M^+, thus exhibiting an excellent Li^+/M^+ separation performance. Theoretical calculations suggest that the interaction of ions with the MXene channels is the key to the selective Li^+ transport, while the stacking order of the MXene nanosheets determines the permeation rate of Li^+. We believe that the proposed strategy paves the way for the preparation of lamellar membranes with controllable sieving performance. The tunable stacking order of the nanosheets in 2D lamellar membranes confirms tremendous opportunity for nanofluidic ion transport and high-efficient molecule sieving from both experimental and theoretical views.

Acknowledgements

We gratefully acknowledge the funding from the National Natural Science Foundation of China (22138005, 22141001, 22378226), Young Elite Scientists Sponsorship Program by BAST. Open Access funding enabled and organized by Projekt DEAL.

Conflict of Interest

The authors declare no conflict of interest.

Data Availability Statement

The data that support the findings of this study are available from the corresponding author upon reasonable request.

Keywords: MXene · Membrane · Monovalent Ion Separation · Nanochannel

[1] a) Y. Sun, Q. Wang, Y. Wang, R. Yun, X. Xiang, *Sep. Purif. Technol.* **2021**, *256*, 117807; b) S. Xu, J. Song, Q. Bi, Q. Chen, W.-M. Zhang, Z. Qian, L. Zhang, S. Xu, N. Tang, T. He, *J. Membr. Sci.* **2021**, *635*, 119441; c) Y. Liu, B. Ma, Y. Lü, C. Wang, Y. Chen, *Int. J. Miner. Metall. Mater.* **2023**, *30*, 209–224.

[2] C. Chen, C.-T. A. Lee, M. Tang, K. Biddle, W. Sun, *Nat. Commun.* **2020**, *11*, 5313.

[3] a) A. Sood, A. D. Poletayev, D. A. Cogswell, P. M. Csernica, J. T. Mefford, D. Fraggedakis, M. F. Toney, A. M. Lindenberg, M. Z. Bazant, W. C. Chueh, *Nat. Rev. Mater.* **2021**, *6*, 847–867; b) C. Liu, Y. Li, D. Lin, P.-C. Hsu, B. Liu, G. Yan, T. Wu, Y. Cui, S. Chu, *Joule* **2020**, *4*, 1459–1469; c) X. Li, Y. Mo, W. Qing, S. Shao, C. Y. Tang, J. Li, *J. Membr. Sci.* **2019**, *591*, 117317.

[4] a) B. E. Logan, M. Elimelech, *Nature* **2012**, *488*, 313–319; b) S. P. Nunes, P. Z. Culfaz-Emecen, G. Z. Ramon, T. Visser, G. H. Koops, W. Jin, M. Ulbricht, *J. Membr. Sci.* **2020**, *598*, 117761; c) M. M. Pendergast, E. M. V. Hoek, *Energy Environ. Sci.* **2011**, *4*, 1946–1971.

[5] a) A. Razmjou, M. Asadnia, E. Hosseini, A. Habibnejad Korayem, V. Chen, *Nat. Commun.* **2019**, *10*, 5793; b) M. L. Vera, W. R. Torres, C. I. Galli, A. Chagnes, V. Flexer, *Nat. Rev. Earth Environ.* **2023**, *4*, 149–165.

[6] a) S. Bing, W. Xian, S. Chen, Y. Song, L. Hou, X. Liu, S. Ma, Q. Sun, L. Zhang, *Matter* **2021**, *4*, 2027–2038; b) Z. Lu, Y. Wu, L. Ding, Y. Wei, H. Wang, *Angew. Chem. Int. Ed.* **2021**, *60*, 22265–22269; c) J. Hou, H. Zhang, A. W. Thornton, A. J. Hill, H. Wang, K. Konstas, *Adv. Funct. Mater.* **2021**, *31*, 2105991; d) T. Gu, R. Zhang, S. Zhang, B. Shi, J. Zhao, Z. Wang, M. Long, G. Wang, T. Qiu, Z. Jiang, *J. Membr. Sci.* **2022**, *659*, 120802; e) F. Sheng, B. Wu, X. Li, T. Xu, M. A. Shehzad, X. Wang, L. Ge, H. Wang, T. Xu, *Adv. Mater.* **2021**, *33*, 2104404.

[7] a) T. Zhang, H. Bai, Y. Zhao, B. Ren, T. Wen, L. Chen, S. Song, S. Komarneni, *ACS Nano* **2022**, *16*, 4930–4939; b) Y.-H. Xi, Z. Liu, J. Ji, Y. Wang, Y. Faraj, Y. Zhu, R. Xie, X.-J. Ju, W. Wang, X. Lu, L.-Y. Chu, *J. Membr. Sci.* **2018**, *550*, 208–218; c) T. Xu, B. Wu, L. Hou, Y. Zhu, F. Sheng, Z. Zhao, Y. Dong, J. Liu, B. Ye, X. Li, L. Ge, H. Wang, T. Xu, *J. Am. Chem. Soc.* **2022**, *144*, 10220–10229; d) J. Abraham, K. S. Vasu, C. D. Williams, K. Gopinadhan, Y. Su, C. T. Cherian, J. Dix, E. Prestat, S. J. Haigh, I. V. Grigorieva, P. Carbone, A. K. Geim, R. R. Nair, *Nat. Nanotechnol.* **2017**, *12*, 546–550; e) E. R. Nightingale Jr., *J. Phys. Chem.* **1959**, *63*, 1381–1387.

[8] Q. Wen, D. Yan, F. Liu, M. Wang, Y. Ling, P. Wang, P. Kluth, D. Schauries, C. Trautmann, P. Apel, W. Guo, G. Xiao, J. Liu, J. Xue, Y. Wang, *Adv. Funct. Mater.* **2016**, *26*, 5796–5803.

[9] a) A. Razmjou, G. Eshaghi, Y. Orooji, E. Hosseini, A. H. Korayem, F. Mohagheghian, Y. Boroumand, A. Noorbakhsh, M. Asadnia, V. Chen, *Water Res.* **2019**, *159*, 313–323; b) H. Zhang, J. Hou, Y. Hu, P. Wang, R. Ou, L. Jiang, J. Z. Liu, B. D. Freeman, A. J. Hill, H. Wang, *Sci. Adv.* **2018**, *4*, eaaq0066.

[10] a) M. Naguib, M. Kurtoglu, V. Presser, J. Lu, J. Niu, M. Heon, L. Hultman, Y. Gogotsi, M. W. Barsoum, *Adv. Mater.* **2011**, *23*, 4248–4253; b) M. Naguib, V. N. Mochalin, M. W. Barsoum, Y. Gogotsi, *Adv. Mater.* **2014**, *26*, 992–1005.

[11] B. Anasori, M. R. Lukatskaya, Y. Gogotsi, *Nat. Rev. Mater.* **2017**, *2*, 16098.

[12] a) L. Ding, Y. Wei, L. Li, T. Zhang, H. Wang, J. Xue, L.-X. Ding, S. Wang, J. Caro, Y. Gogotsi, *Nat. Commun.* **2018**, *9*, 155; b) J. Shen, G. Liu, Y. Ji, Q. Liu, L. Cheng, K. Guan, M. Zhang, G. Liu, J. Xiong, J. Yang, W. Jin, *Adv. Funct. Mater.* **2018**, *28*, 1801511.

[13] L. Ding, L. Li, Y. Liu, Y. Wu, Z. Lu, J. Deng, Y. Wei, J. Caro, H. Wang, *Nat. Sustainability* **2020**, *3*, 296–302.

[14] a) Z. Zhang, S. Yang, P. Zhang, J. Zhang, G. Chen, X. Feng, *Nat. Commun.* **2019**, *10*, 2920; b) Y. Wang, H. Zhang, Y. Kang, Y. Zhu, G. P. Simon, H. Wang, *ACS Nano* **2019**, *13*, 11793–11799.

[15] a) L. Ding, Y. Wei, Y. Wang, H. Chen, J. Caro, H. Wang, *Angew. Chem. Int. Ed.* **2017**, *56*, 1825–1829; b) Z. Lu, Y. Wei, J. Deng, L. Ding, Z.-K. Li, H. Wang, *ACS Nano* **2019**, *13*, 10535–10544.

[16] P. A. Forsyth, S. Marčelja, D. J. Mitchell, B. W. Ninham, *J. Chem. Soc. Faraday Trans. 2* **1977**, *73*, 84–88.

[17] J. Zhang, N. Kong, S. Uzun, A. Levitt, S. Seyedin, P. A. Lynch, S. Qin, M. Han, W. Yang, J. Liu, X. Wang, Y. Gogotsi, J. M. Razal, *Adv. Mater.* **2020**, *32*, 2001093.

[18] a) C. J. Zhang, S. Pinilla, N. McEyoy, C. P. Cullen, B. Anasori, E. Long, S.-H. Park, A. Seral-Ascaso, A. Shmeliov, D. Krishnan, C. Morant, X. Liu, G. S. Duesberg, Y. Gogotsi, V. Nicolosi, *Chem. Mater.* **2017**, *29*, 4848–4856; b) K. Hantanasirisakul, M.-Q. Zhao, P. Urbankowski, J. Halim, B. Anasori, S. Kota, C. E. Ren, M. W. Barsoum, Y. Gogotsi, *Adv. Electron. Mater.* **2016**, *2*, 1600050.

[19] R. Mezzenga, C. Meyer, C. Servais, A. I. Romoscanu, L. Sagalowicz, R. C. Hayward, *Langmuir* **2005**, *21*, 3322–3333.

[20] a) B. Akuzum, K. Maleski, B. Anasori, P. Lelyukh, N. J. Alvarez, E. C. Kumbur, Y. Gogotsi, *ACS Nano* **2018**, *12*, 2685–2694; b) Y. Zhao, Q. Yu, W.-W. Cheng, J.-Q. Li, A.-Q. Zhang, X. Lei, Y. Yang, S.-Y. Qin, *ACS Nano* **2022**, *16*, 5454–5462.

[21] a) R. Tkacz, R. Oldenbourg, A. Fulcher, M. Miansari, M. Majumder, *J. Phys. Chem. C* **2014**, *118*, 259–267; b) A. Akbari, P. Sheath, S. T. Martin, D. B. Shinde, M. Shaibani, P. C. Banerjee, R. Tkacz, D. Bhattacharyya, M. Majumder, *Nat. Commun.* **2016**, *7*, 10891.

[22] H. Wang, Y. Zhai, Y. Li, Y. Cao, B. Shi, R. Li, Z. Zhu, H. Jiang, Z. Guo, M. Wang, L. Chen, Y. Liu, K.-G. Zhou, F. Pan, Z. Jiang, *Nat. Commun.* **2022**, *13*, 7123.

[23] C. E. Ren, K. B. Hatzell, M. Alhabeb, Z. Ling, K. A. Mahmoud, Y. Gogotsi, *J. Phys. Chem. Lett.* **2015**, *6*, 4026–4031.

[24] a) J. Lu, H. Zhang, J. Hou, X. Li, X. Hu, Y. Hu, C. D. Easton, Q. Li, C. Sun, A. W. Thornton, M. R. Hill, X. Zhang, G. Jiang, J. Z. Liu, A. J. Hill, B. D. Freeman, L. Jiang, H. Wang, *Nat. Mater.* **2020**, *19*, 767–774; b) C. Zhang, Y. Mu, W. Zhang, S. Zhao, Y. Wang, *J. Membr. Sci.* **2020**, *596*, 117724; c) X. Shi, Z. Zhang, S. Fang, J. Wang, Y. Zhang, Y. Wang, *Nano Lett.* **2021**, *21*, 8355–8362; d) W. Xin, C. Lin, L. Fu, X.-Y. Kong, L. Yang, Y. Qian, C. Zhu, Q. Zhang, L. Jiang, L. Wen, *Matter* **2021**, *4*, 737–754; e) R. Tan, A. Wang, R. Malpass-Evans, R. Williams, E. W. Zhao, T. Liu, C. Ye, X. Zhou, B. P. Darwich, Z. Fan, L. Turcani, E. Jackson, L. Chen, S. Y. Chong, T. Li, K. E. Jelfs, A. I. Cooper, N. P. Brandon, C. P. Grey, N. B. McKeown, Q. Song, *Nat. Mater.* **2020**, *19*, 195–202; f) P. Wang, M. Wang, F. Liu, S. Ding, X. Wang, G. Du, J. Liu, P. Apel, P. Kluth, C. Trautmann, Y. Wang, *Nat. Commun.* **2018**, *9*, 569.

[25] F. Arshadi, M. Mohammad, E. Hosseini, H. Ahmadi, M. Asadnia, Y. Orooji, A. H. Korayem, A. Noorbakhsh, A. Razmjou, *J. Membr. Sci.* **2021**, *639*, 119752.

[26] Q. Gao, W. Sun, P. Ilani-Kashkouli, A. Tselev, P. R. C. Kent, N. Kabengi, M. Naguib, M. Alhabeb, W.-Y. Tsai, A. P. Baddorf, J. Huang, S. Jesse, Y. Gogotsi, N. Balke, *Energy Environ. Sci.* **2020**, *13*, 2549–2558.

Manuscript received: September 29, 2023
Accepted manuscript online: November 27, 2023
Version of record online: January 4, 2024